On bounded approximations of periodicity for computational homogenization of Stokes flow in porous media

INTERNATIONAL JOURNAL FOR NUMERICAL METHODS IN ENGINEERING
Int. J. Numer. Meth. Engng 2017; **109**:307–325
Published online 30 June 2016 in Wiley Online Library (wileyonlinelibrary.com). DOI: 10.1002/nme.5281

On bounded approximations of periodicity for computational homogenization of Stokes flow in porous media

Carl Sandström*,† and Fredrik Larsson

Chalmers University of Technology, Dept. of Applied Mechanics, SE41296 Sweden

SUMMARY

By separation of scales and the homogenization of a flow through porous media, a two-scale problem arises where a Darcy-type flow is present on the macroscale and a Stokes flow on the subscale. In this paper, the problem is given as the minimization of a potential. Additional constraints imposing periodicity in a weak sense are added using Lagrange multipliers. In particular, the upper and lower energy bounds for the corresponding strongly periodic problem are produced, quantifying the accuracy of the weakly periodic boundary conditions. A numerical example demonstrates the evaluation of energy bounds and the performance of weakly periodic boundary conditions on a representative volume element. © 2016 The Authors. *International Journal for Numerical Methods in Engineering* Published by John Wiley & Sons Ltd.

Received 17 March 2015; Revised 9 March 2016; Accepted 8 April 2016

KEY WORDS: incompressible flow; multiscale; viscous flow; finite element methods; permeability; bounds

1. INTRODUCTION

In this paper, we consider the two-scale problem where a Stokes flow is present on the subscale and a Darcy flow on the macroscale. Thus, the macroscale is considered homogeneous, while the subscale is considered porous, that is, it consists of a solid and a fluid phase. The two-scale approach used to simulate the behavior of materials is common for a large number of engineering applications including oil geology [1], sintering [2], resin transfer modeling [3, 4], and transportation of matter [5] to name a few.

The objective for models of this type, known as multiscale models, is to capture the subscale effects without the computational effort involved in resolving the complete microstructure. To that end, computational homogenization [6] is employed. Here, a representative volume element (RVE), containing a suitably large volume of the microstructure, is used as a replacement for the classic phenomenological model pertinent to the macroscale problem, that is, a Darcy flow. A Stokes flow is present on the RVE, which is driven by the macroscale pressure gradient. The resulting macroscale seepage is computed using volume averaging of the velocity on the RVE. In this work, the solid part of the porous material is considered rigid.

The derivation of a Darcy flow from a subscale Stokes flow can be found in, for example, [7–9]. Previous work concerning the upper and lower energy bounds of a Darcy flow can be found in [10] and [11] where various kinds of correlation functions, describing the characteristics of the microstructure, are used to estimate the bounds. In this paper, the bounds produced using weak periodicity [12], which allows for handling non-periodic meshes.

*Correspondence to: Carl Sandström, Applied Mechanics, Material and Computational Mechanics, Hörsalsvägen 7B, Gothenburg 41258, Sweden.

†E-mail: carl.sandstrom@chalmers.se

We consider the variationally consistent homogenization (VCH) method as a framework for the multiscale model. VCH is an extension of variational multiscale method (VMS) proposed by Hughes and coworkers [13, 14]. The more classic format of VMS has also been used on a Stokes flow as shown in [15]. The extension of VMS to VCH was first proposed by Larsson et al. [16], where the pertinent generalized macrohomogeneity condition was introduced for guaranteeing energy equivalence for the homogenized response.

Following along the lines of Sandström *et al.* [12], we consider a viscous potential on a fully resolved domain consisting of a fluid phase contained within a rigid and geometrically periodic open pore solid. By splitting the domain into a finite number of subdomains and assuming separation of scales, we define the geometry and size of the pertinent RVE. From here, we use, as an approximation, periodic boundary conditions that, as shown in [17], satisfy the variationally consistent macrohomogeneity condition. In other words, we ensure energy equivalence on macroscale and subscale [16]. In particular, we impose periodic boundary conditions in weak form, resulting in additional unknown Lagrange multipliers on the RVE. The unknowns constitute external loads necessary to uphold periodicity on the pertinent fields.

By minimizing a viscous potential on the RVE, a saddle point problem is produced, allowing for the analysis of upper and lower energy bounds for the strongly periodic problem. The bounds are produced by confining pertinent solution spaces to contain only strongly periodic velocities or pressures. In a 2D setting, this can be achieved using quadratic interpolation over each opening on the boundary because the boundary is 1D [12]. In this way, we allow for the fluid to enter and exit the RVE while satisfying the no-slip condition on obstacles crossing the boundary. However, as the geometry of the surface of the RVE in 3D is of arbitrary 2D shape, the choice of global base functions is not as straightforward.

As a suggestion for the choice of basis functions on the 2D surface, we introduce the concept of solution-based shape functions. To compute the shape functions, we use a possibly non-periodic solution of a Stokes flow to produce an analytically periodic function. The function is then projected onto the boundary, producing a function that is periodic up to the error introduced by the discretization of the domain while satisfying no-slip conditions. We note that this procedure is used on the velocity to produce an upper bound and on the pressure to produce a lower bound. In the case of velocity, a method for compensating for possible compressibility artifacts due to the prescribed inflow on all open boundaries is also discussed. We note that an important part of this paper concerns the weak periodic boundary condition [12]. In [18], an alternative approach to weak boundary conditions is discussed.

The outline of the remainder of this paper is as follows. In Section 2, we start out from the energy formulation and derive the weak form of the problem. In Section 3, the upper and lower energy bounds are discussed and for the special case of linear flow, the permeability. In Section 4, a general method for producing function spaces pertinent to the bounds is shown along with special handling of incompressibility. The function spaces for the bounds are studied in more detail in Section 4.2 for the upper energy bounds and in Section 4.3, for the lower bound. Section 5 contains a numerical example of a simple RVE where the bounds are computed and the performance of the weak periodic boundary condition is evaluated. In Section 6, we finish the paper with some concluding remarks and suggestions for future work.

2. PROBLEM FORMULATION

2.1. Multiscale Stokes flow – the saddle point problem

In this section, we provide the reader with the basic background on the two scale problem and the pertinent boundary conditions.

For the subsequent two-scale problem, we introduce the macroscale domain Ω and the RVE $\Omega_\square$. The boundary $\Gamma = \partial\Omega$ of the macroscale domain is split into two parts, $\Gamma = \Gamma_v \cup \Gamma_p$, where Γ_p is the part where the pressure is prescribed and Γ_v is the part where the out-flux is prescribed. The RVE consists of two subdomains $\Omega_\square = \Omega_\square^{\mathrm{F}} \cup \Omega_\square^{\mathrm{S}}$ where $\Omega_\square^{\mathrm{F}}$ is the volume containing the fluid and $\Omega_\square^{\mathrm{S}}$ the volume containing the solid phase, as shown in Figure 1. The solid phase is considered

DOI: 10.1002/nme

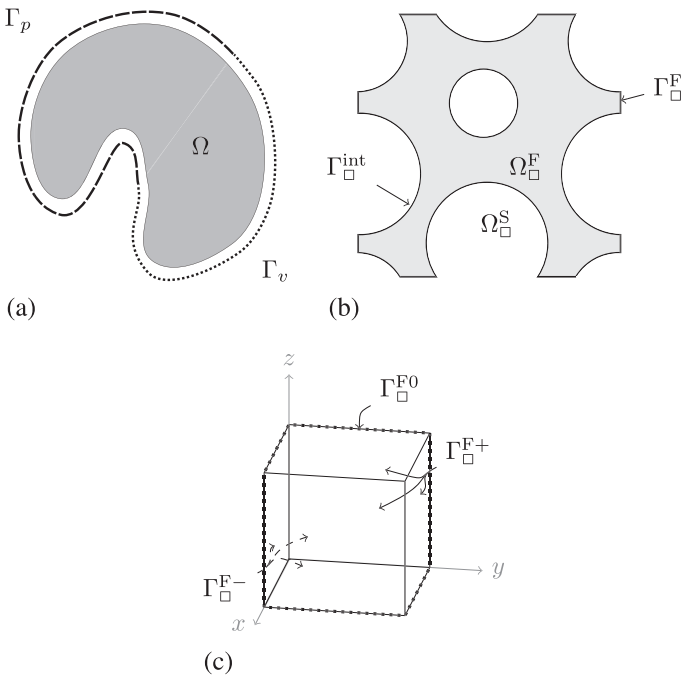

Figure 1. (a) Macroscale; (b) subscale; and (c) positive and negative parts of the boundary.

rigid, and the interface between the two phases is denoted $\Gamma^{\mathrm{int}}_{\square}$. $\Gamma^{\mathrm{F}}_{\square}$ is the part of $\partial\Omega_{\square}$ where fluid can enter and exit the domain. For reasons given momentarily, we also denote the part of $\Omega^{\mathrm{F}}_{\square}$ having a normal in a positive direction as $\Gamma^{\mathrm{F+}}_{\square}$ and for part having a normal in the negative direction as $\Gamma^{\mathrm{F-}}_{\square}$. Finally, we also define the boundary between $\Gamma^{\mathrm{F+}}_{\square}$ and $\Gamma^{\mathrm{F-}}_{\square}$ as $\Gamma^{\mathrm{F0}}_{\square} = \Gamma^{\mathrm{F+}}_{\square} \cap \Gamma^{\mathrm{F-}}_{\square}$ as shown in Figure 1(c).

In order to establish a coupling between the macroscale and the subscale, we first define the pressure p on both scales. The pressure p on the RVE is then split into two parts, $p = p^{\mathrm{M}} + p^{\mathrm{S}}$, where p^{M} is the smooth macroscale part and p^{S} is the fluctuating subscale part. Furthermore, we introduce the macroscale pressure $\bar{p}$ and the macroscale pressure gradient $\bar{\boldsymbol{g}}$. As first-order homogenization is assumed, p^{M} is allowed to vary linearly within the RVE as

$$p^{\mathrm{M}} = \bar{p} + \bar{\boldsymbol{g}} \cdot \left[\boldsymbol{x} - \bar{\boldsymbol{x}}^{\mathrm{F}}\right] \tag{1}$$

where $\boldsymbol{x}$ is the coordinate and $\bar{\boldsymbol{x}}^{\mathrm{F}}$ is the centroid of the fluid part of the RVE. From Equation (1), we conclude the macroscale–subscale coupling as $\bar{\boldsymbol{g}} = \boldsymbol{\nabla} p^{\mathrm{M}}$. For a discussion concerning the uniqueness of the split, we refer to [17].

The macroscale problem is given on strong form as

$$\boldsymbol{\nabla} \cdot \bar{\boldsymbol{w}}\left\{\bar{\boldsymbol{g}}\right\} = 0 \tag{2a}$$

$$\bar{p} = \hat{p} \text{ on } \Gamma_p \tag{2b}$$

$$\bar{\boldsymbol{w}} \cdot \boldsymbol{n} = \hat{v}_n \text{ on } \Gamma_v \tag{2c}$$

where $\bar{\boldsymbol{w}}$ is the seepage, $\boldsymbol{n}$ is the outward pointing normal to the boundary, $\hat{p}$ is a prescribed pressure, and $\hat{v}_n$ is the prescribed flux in the outward pointing normal direction of Γ_v. Furthermore, $\{\bullet\}$ denotes implicit dependence on $\bullet$.

We define the seepage $\bar{\boldsymbol{w}}$ in terms of the stationary mean RVE potential $\psi_{\square}\left\{\bar{\boldsymbol{g}}\right\}$

$$\bar{\boldsymbol{w}} = \frac{\partial \psi_{\square}}{\partial \bar{\boldsymbol{g}}} \tag{3}$$

In the case of a laminar, incompressible, and strongly periodic flow, the potential $\psi_{\square}$ is given as a stationary point to the optimization problem

DOI: 10.1002/nme

$$\psi_{\square}\{\bar{\boldsymbol{g}}\} = \inf_{\boldsymbol{v}\in\mathcal{V}_{\square}^{\mathrm{P}}} \sup_{p^{\mathrm{S}}\in\mathcal{P}_{\square}^{\mathrm{S,P}}} \frac{1}{|\Omega_{\square}|}\left\{\int_{\Omega_{\square}^{\mathrm{F}}} \Phi(\boldsymbol{v}\otimes\boldsymbol{\nabla})\mathrm{d}V - \int_{\Omega_{\square}^{\mathrm{F}}} p^{\mathrm{S}}(\boldsymbol{\nabla}\cdot\boldsymbol{v})\mathrm{d}V + \int_{\Omega_{\square}^{\mathrm{F}}} \boldsymbol{v}\cdot\bar{\boldsymbol{g}}\,\mathrm{d}V - \int_{\Gamma_{\square}^{\mathrm{F}}} \boldsymbol{t}^{S}\cdot\boldsymbol{v}\mathrm{d}V\right\} \tag{4}$$

where $\boldsymbol{v}$ is the velocity of a fluid particle, the subscale pressure p^{S} is a Lagrange multiplier due to the incompressibility condition, and $\Phi(l)$ is a viscous potential (expressed in terms of the velocity gradient $\boldsymbol{l} = \boldsymbol{v}\otimes\boldsymbol{\nabla}$), such that $\frac{\partial\Phi}{\partial\boldsymbol{l}} = \boldsymbol{\sigma}^{\mathrm{V}}$ being the deviatoric part of the Cauchy stress. The solution spaces in Equation (4) are defined as

$$\mathcal{V}_{\square}^{\mathrm{P}} = \left\{\boldsymbol{v} : \boldsymbol{v}\in\mathcal{V}_{\square}, \boldsymbol{v} \text{ is periodic on } \Gamma_{\square}^{\mathrm{F}}\right\} \tag{5a}$$

$$\mathcal{P}_{\square}^{\mathrm{S,P}} = \left\{p : p\in\mathcal{P}_{\square}^{\mathrm{S}}, p \text{ is periodic on } \Gamma_{\square}^{\mathrm{F}}\right\} \tag{5b}$$

where

$$\mathcal{V}_{\square} = \left\{\boldsymbol{v}\in[H^1(\Omega^{\mathrm{F}})]^3 : \boldsymbol{v} = \boldsymbol{0} \text{ on } \Gamma_{\square}^{\mathrm{int}}\right\} \tag{6a}$$

$$\mathcal{P}_{\square}^{\mathrm{S}} = \left\{p\in H^1\left(\Omega_{\square}^{\mathrm{F}}\right)\right\} \tag{6b}$$

As a final remark on the potential, we note that $\boldsymbol{t}^{S} = (\boldsymbol{\sigma}^{\mathrm{V}} - p^{\mathrm{S}}\mathbf{I})\cdot\boldsymbol{n}$ is the traction pertinent to the reaction forces due to split of Ω into a finite number of RVEs. Henceforth, we will neglect this term as it is zero when the macrohomogeneity condition is fulfilled. For further reading on this topic, we refer to [17].

For the special case of linear flow, we have the viscous stress $\boldsymbol{\sigma}^{\mathrm{V}}$ defined as

$$\boldsymbol{\sigma}^{\mathrm{V}} = 2\mu[\boldsymbol{v}\otimes\boldsymbol{\nabla}]^{\mathrm{sym}} \tag{7}$$

2.2. *Weak periodicity on the RVE using Lagrange multipliers*

We will now weaken the conditions on $\boldsymbol{v}$ and p^{S} by using the larger function spaces $\mathcal{V}_{\square}$ and $\mathcal{P}_{\square}^{\mathrm{S}}$ as replacements for $\mathcal{V}_{\square}^{\mathrm{P}}$ and $\mathcal{P}_{\square}^{\mathrm{S,P}}$ and instead impose periodicity on the pressure and velocity fields on the RVE in a weak sense. For this purpose, we introduce the jump operator $[\![\bullet]\!]$ as

$$[\![f]\!] = f(\boldsymbol{x}) - f(\boldsymbol{x}^{-}(\boldsymbol{x})) \tag{8}$$

where $\boldsymbol{x}\in\Gamma_{\square}^{\mathrm{F}+}$ and $\boldsymbol{x}^{-}(\boldsymbol{x})$ are the corresponding points on $\Gamma_{\square}^{\mathrm{F}-}$. When enforcing periodicity, we do so by manipulating the stationary mean RVE potential $\psi_{\square}$ in Equation (4). Thus, we add the conditions

$$[\![p^{\mathrm{S}}]\!] = 0 \tag{9a}$$

$$[\![\boldsymbol{v}]\!] = \boldsymbol{0} \tag{9b}$$

$$\boldsymbol{t}^{\mathrm{S}+} + \boldsymbol{t}^{\mathrm{S}-} = \boldsymbol{0} \tag{9c}$$

where $\boldsymbol{t}^{\mathrm{S}+}$ and $\boldsymbol{t}^{\mathrm{S}-}$ are tractions along $\Gamma_{\square}^{\mathrm{F}+}$ and $\Gamma_{\square}^{\mathrm{F}-}$, respectively. As the conditions enter into the optimization problem, they give rise to Lagrange multiplier $\boldsymbol{\beta}$ for the velocity constraint and γ for the pressure constraint. The stationary mean RVE potential now takes the form

$$\psi_{\square}(\bar{\boldsymbol{g}}) = \inf_{\boldsymbol{v}\in\mathcal{V}_{\square}} \sup_{\substack{p^{\mathrm{S}}\in\mathcal{P}_{\square}^{\mathrm{S}}\\ \boldsymbol{\beta}\in\mathcal{B}_{\square}}} \inf_{\gamma\in\mathcal{G}_{\square}} \pi_{\square}\left(\boldsymbol{v}, p^{\mathrm{S}}, \boldsymbol{\beta}, \gamma, \bar{\boldsymbol{g}}\right) \tag{10}$$

DOI: 10.1002/nme

where $\pi_\square$ is the mean RVE potential, defined as

$$\begin{aligned}&\pi_\square\left(\boldsymbol{v}, p^{\mathrm{S}}, \boldsymbol{\beta}, \gamma, \bar{\boldsymbol{g}}\right)\\&= \frac{1}{|\Omega_\square|}\left(\int_{\Omega_\square^{\mathrm{F}}} \Phi(\boldsymbol{v}\otimes\nabla)\mathrm{d}V - \int_{\Omega_\square^{\mathrm{F}}} p^{\mathrm{S}}(\nabla\cdot\boldsymbol{v})\mathrm{d}V + \int_{\Omega_\square^{\mathrm{F}}} \bar{\boldsymbol{g}}\cdot\boldsymbol{v}\mathrm{d}V - \int_{\Gamma_\square^{\mathrm{F}+}} [\![\boldsymbol{v}]\!]\cdot\boldsymbol{\beta} + [\![p^{\mathrm{S}}]\!]\gamma\mathrm{d}S\right)\end{aligned} \tag{11}$$

and

$$\mathcal{B}_\square = \left\{\boldsymbol{\beta} \in \left[L_2\left(\Gamma_\square^{\mathrm{F}+}\right)\right]^3\right\} \tag{12a}$$

$$\mathcal{G}_\square = \left\{\gamma \in L_2\left(\Gamma_\square^{\mathrm{F}+}\right)\right\} \tag{12b}$$

For the situation in Equation (10), we note that the seepage satisfies

$$\bar{\boldsymbol{w}}\cdot\delta\bar{\boldsymbol{g}} = \frac{\mathrm{d}\psi_\square}{\mathrm{d}\bar{\boldsymbol{g}}} = \pi'_\square\left(\boldsymbol{v}, p^{\mathrm{S}}, \boldsymbol{\beta}, \gamma, \bar{\boldsymbol{g}}; \delta\bar{\boldsymbol{g}}\right) \tag{13}$$

due to the stationarity of $\pi_\square$ (cf. [12]). Here, $\pi'_\square$ denotes the directional derivative of $\pi_\square$ w.r.t. $\bar{\boldsymbol{g}}$ in the direction of $\delta\bar{\boldsymbol{g}}$.

Remark 1
The solution to Equation (10) can be stated as

$$\left(\boldsymbol{v}\left\{\bar{\boldsymbol{g}}\right\}, p^{\mathrm{S}}\left\{\bar{\boldsymbol{g}}\right\}, \boldsymbol{\beta}\left\{\bar{\boldsymbol{g}}\right\}, \gamma\left\{\bar{\boldsymbol{g}}\right\}\right) = \arg\min_{\boldsymbol{v}\in\mathcal{V}_\square}\max_{\substack{p^{\mathrm{S}}\in\mathcal{P}_\square\\ \boldsymbol{\beta}\in\mathcal{B}}}\min_{\gamma\in\mathcal{G}} \psi_\square\left(\boldsymbol{v}, p^{\mathrm{S}}, \boldsymbol{\beta}, \gamma, \bar{\boldsymbol{g}}\right) \tag{14}$$

if we assume a unique solution. Consequently, the explicit description of the stationary RVE problem becomes

$$\psi_\square\left\{\bar{\boldsymbol{g}}\right\} = \pi_\square\left(\boldsymbol{v}\left\{\bar{\boldsymbol{g}}\right\}, p^{\mathrm{S}}\left\{\bar{\boldsymbol{g}}\right\}, \boldsymbol{\beta}\left\{\bar{\boldsymbol{g}}\right\}, \gamma\left\{\bar{\boldsymbol{g}}\right\}\right) \tag{15}$$

We stress that the existence of a unique solution $\left(\boldsymbol{v}\left\{\bar{\boldsymbol{g}}\right\}, p^{\mathrm{S}}\left\{\bar{\boldsymbol{g}}\right\}, \boldsymbol{\beta}\left\{\bar{\boldsymbol{g}}\right\}, \gamma\left\{\bar{\boldsymbol{g}}\right\}\right)$ is a stronger requirement than the formulation in Equation (10).

Remark 2
We note that by using the definition of the split and first-order homogenization, the periodicity condition on the subscale pressure p^{S} is equivalent to the condition

$$[\![p]\!] = \bar{\boldsymbol{g}}\cdot[\![\boldsymbol{x}]\!] \tag{16}$$

Thus, we can rewrite Equation (11) as

$$\begin{aligned}&\pi_\square\left(\boldsymbol{v}, p, \boldsymbol{\beta}, \gamma, \bar{\boldsymbol{g}}\right)\\&= \frac{1}{|\Omega_\square|}\left(\int_{\Omega_\square^{\mathrm{F}}} \Phi(\boldsymbol{v}\otimes\nabla)\mathrm{d}V - \int_{\Omega_\square^{\mathrm{F}}} p(\nabla\cdot\boldsymbol{v})\mathrm{d}V - \int_{\Gamma_\square^{\mathrm{F}+}} [\![\boldsymbol{v}]\!]\cdot\boldsymbol{\beta}\right.\\&\qquad\left. + [\![p - \bar{\boldsymbol{g}}\cdot\boldsymbol{x}]\!]\gamma\mathrm{d}S - \int_{\Gamma_\square^{\mathrm{F}}}\left(\bar{\boldsymbol{g}}\cdot[\boldsymbol{x}-\boldsymbol{x}^F]\right)\boldsymbol{n}\cdot\boldsymbol{v}\mathrm{d}S\right)\end{aligned} \tag{17}$$

Here, the split of the domain into RVEs gives the traction $\boldsymbol{t} = \boldsymbol{t}^{\mathrm{S}} - \bar{\boldsymbol{g}}\cdot[\boldsymbol{x}-\boldsymbol{x}^F]\cdot\boldsymbol{n}$ on the boundary. Assuming that the integral containing the subscale traction $\boldsymbol{t}^{\mathrm{S}}$ vanishes because of boundary conditions satisfying the variationally consistent macrohomogeneity condition, we obtain the last integral in Equation (17). This formulation allows for the computation of the full pressure up to a constant rather than the subscale pressure p^{S}.

DOI: 10.1002/nme

2.3. Weak form

For the weak form of the macroscale equation, we refer to [12] and proceed by taking variations in all subscale quantities in Equation (11), producing the following weak form of the subscale problem: Find $(\boldsymbol{v}, p^{\mathrm{S}}, \boldsymbol{\beta}, \gamma) \in \mathcal{V}_\square \times \mathcal{P}^{\mathrm{S}}_\square \times \mathcal{B}_\square \times \mathcal{G}_\square$ such that

$$
\begin{aligned}
a_\square(\boldsymbol{v};\delta\boldsymbol{v}) - b_\square(\delta\boldsymbol{v}, p^{\mathrm{S}}) \quad -c_\square(\delta\boldsymbol{v},\boldsymbol{\beta}) \qquad\qquad &= -e_\square(\delta\boldsymbol{v},\bar{\boldsymbol{g}}) \qquad \forall\delta\boldsymbol{v}\in\mathcal{V}_\square \quad (18a)\\
-b_\square\left(\boldsymbol{v},\delta p^{\mathrm{S}}\right) \qquad\qquad - d_\square\left(\delta p^{\mathrm{S}},\gamma\right) &= 0 \qquad \forall\delta p^{\mathrm{S}}\in\mathcal{P}^{\mathrm{S}}_\square \quad (18b)\\
-c_\square(\boldsymbol{v},\delta\boldsymbol{\beta}) \qquad\qquad &= 0 \qquad \forall\delta\boldsymbol{\beta}\in\mathcal{B}_\square \quad (18c)\\
- d_\square\left(p^{\mathrm{S}},\delta\gamma\right) &= 0 \qquad \forall\delta\gamma\in\mathcal{G}_\square \quad (18d)
\end{aligned}
$$

where

$$a_\square(\boldsymbol{v};\delta\boldsymbol{v}) = \frac{1}{|\Omega_\square|}\int_{\Omega^{\mathrm{F}}_\square}\boldsymbol{\sigma}^{\mathrm{V}}(\boldsymbol{v}\otimes\boldsymbol{\nabla}) : [\delta\boldsymbol{v}\otimes\boldsymbol{\nabla}]\mathrm{d}V \tag{19a}$$

$$b_\square\left(\delta\boldsymbol{v}, p^{\mathrm{S}}\right) = \frac{1}{|\Omega_\square|}\int_{\Omega^{\mathrm{F}}_\square}[\delta\boldsymbol{v}\cdot\boldsymbol{\nabla}]p^{\mathrm{S}}\mathrm{d}V \tag{19b}$$

$$c_\square(\delta\boldsymbol{v},\boldsymbol{\beta}) = \frac{1}{|\Omega_\square|}\int_{\Gamma^{\mathrm{F}}_\square}[\![\delta\boldsymbol{v}]\!]\cdot\boldsymbol{\beta}\mathrm{d}S \tag{19c}$$

$$d_\square(\delta p,\gamma) = \frac{1}{|\Omega_\square|}\int_{\Gamma^{\mathrm{F}}_\square}[\![\delta p^{\mathrm{S}}]\!]\gamma\mathrm{d}S \tag{19d}$$

$$e_\square(\delta\boldsymbol{v},\bar{\boldsymbol{g}}) = \frac{1}{|\Omega_\square|}\int_{\Omega^{\mathrm{F}}_\square}\delta\boldsymbol{v}\mathrm{d}V\cdot\bar{\boldsymbol{g}} \tag{19e}$$

In Equation (18a), the known macroscale pressure gradient $\bar{\boldsymbol{g}}$ acts as a driving load for the flow.

Remark 3
In a discrete setting, the tangent stiffness of Equation (18) is a block matrix

$$\mathbf{T} = \begin{bmatrix} \mathbf{A} & \mathbf{G} & \mathbf{C} & \\ \mathbf{G}^{\mathrm{T}} & & & \mathbf{D} \\ \mathbf{C}^{\mathrm{T}} & & & \\ & & \mathbf{D}^{\mathrm{T}} & \end{bmatrix} \tag{20}$$

where submatrices $\mathbf{C}$ and $\mathbf{D}$ constitute the weak boundary conditions. In the case where relevant base functions are global, the submatrices can be considered dense. As a result, the computational cost increases rapidly as the Lagrange multiplier approximations are refined.

3. ENERGY BOUNDS ON THE PERIODIC SOLUTION

3.1. Confining the solution spaces

From Equation (10), we note that by confining the function spaces in certain ways, we can compute the upper and lower energy bounds. In the special case of a linear fluid material, we are also able to compute upper and lower bounds for the permeability. By replacing $\mathcal{V}_\square$ with $\mathcal{V}'_\square \subset \mathcal{V}_\square$ and $\mathcal{G}_\square$ with $\mathcal{G}'_\square \subset \mathcal{G}_\square$, we produce an upper energy bound. More specifically, by choosing $\mathcal{V}'_\square$ to contain only strongly periodic functions, we produce an upper bound for strongly periodic velocities. This also voids the supremum on $\boldsymbol{\beta}$. The subspace $\mathcal{G}'_\square$ contains the discretized γ, giving the inequality

$$\psi_\square\left(p^{\mathrm{M}}\right) = \inf_{\boldsymbol{v}\in\mathcal{V}_\square}\sup_{\substack{p^{\mathrm{S}}\in\mathcal{P}^{\mathrm{S}}_\square\\ \boldsymbol{\beta}\in\mathcal{B}_\square}}\inf_{\gamma\in\mathcal{G}_\square}\pi_\square\left(\boldsymbol{v},p^{\mathrm{M}},p^{\mathrm{S}},\boldsymbol{\beta},\gamma\right) \leqslant \inf_{\boldsymbol{v}\in\mathcal{V}'_\square}\sup_{p^{\mathrm{S}}\in\mathcal{P}^{\mathrm{S}}_\square}\inf_{\gamma\in\mathcal{G}'_\square}\pi_\square\left(\boldsymbol{v},p^{\mathrm{M}},p^{\mathrm{S}},\boldsymbol{\beta},\gamma\right) = \psi^U_\square\left(p^{\mathrm{M}}\right) \tag{21}$$

DOI: 10.1002/nme

By the same reasoning, we replace the function spaces $\mathcal{P}^{\mathrm{S}}_{\square}$ and $\mathcal{B}_{\square}$ with $\mathcal{P}^{\mathrm{S}\,\prime}_{\square}$ and $\mathcal{B}'_{\square}$, where the particular choice of $\mathcal{P}^{\mathrm{S}\,\prime}_{\square}$ only contains strongly periodic pressures. This yields the inequality pertinent to the lower energy bound for strong periodicity as

$$\psi^{L}_{\square}\left(p^{\mathrm{M}}\right) = \inf_{\boldsymbol{v}\in\mathcal{V}_{\square}} \sup_{\substack{p^{\mathrm{S}}\in\mathcal{P}^{\mathrm{S}\,\prime}_{\square} \\ \boldsymbol{\beta}\in\mathcal{B}'_{\square}}} \pi_{\square}\left(\boldsymbol{v}, p^{\mathrm{M}}, p^{\mathrm{S}}, \boldsymbol{\beta}, \gamma\right) \leqslant \inf_{\boldsymbol{v}\in\mathcal{V}_{\square}} \sup_{\substack{p^{\mathrm{S}}\in\mathcal{P}^{\mathrm{S}}_{\square} \\ \boldsymbol{\beta}\in\mathcal{B}_{\square}}} \inf_{\gamma\in\mathcal{G}_{\square}} \pi_{\square}\left(\boldsymbol{v}, p^{\mathrm{M}}, p^{\mathrm{S}}, \boldsymbol{\beta}, \gamma\right) = \psi_{\square}\left(p^{\mathrm{M}}\right) \tag{22}$$

Summing Equations (21) and (22) gives the bounds on strong periodicity as

$$\psi^{L}_{\square}\left(p^{\mathrm{M}}\right) \leqslant \psi_{\square}\left(p^{\mathrm{M}}\right) \leqslant \psi^{U}_{\square}\left(p^{\mathrm{M}}\right) \tag{23}$$

3.2. Permeability and energy relation in the linear case

In the special case where we have a linear fluid, we have from [12] the following relations between the energy potential on the RVE and the permeability $\bar{\boldsymbol{K}}$

$$\psi^{\mathrm{L}}_{\square}\left(\bar{\boldsymbol{g}}\right) = -\frac{1}{2}\bar{\boldsymbol{g}}\cdot\bar{\boldsymbol{K}}^{\mathrm{U}}\cdot\bar{\boldsymbol{g}} \tag{24a}$$

$$\psi_{\square}\left(\bar{\boldsymbol{g}}\right) = -\frac{1}{2}\bar{\boldsymbol{g}}\cdot\bar{\boldsymbol{K}}\cdot\bar{\boldsymbol{g}} \tag{24b}$$

$$\psi^{\mathrm{U}}_{\square}\left(\bar{\boldsymbol{g}}\right) = -\frac{1}{2}\bar{\boldsymbol{g}}\cdot\bar{\boldsymbol{K}}^{\mathrm{L}}\cdot\bar{\boldsymbol{g}} \tag{24c}$$

Here, the permeability $\bar{\boldsymbol{K}}$ is computed as

$$\bar{\boldsymbol{K}} = -\phi\left(\sum_{i=1}^{3}\left\langle\boldsymbol{v}^{(i)}\right\rangle_{\square}\otimes\boldsymbol{e}_i\right) \tag{25}$$

where $\boldsymbol{v}^{(i)}$ is the velocity field pertinent to a unit pressure gradient $\bar{\boldsymbol{g}}$ in the ith spatial direction. $\langle\bullet\rangle_{\square}$ is the intrinsic averaging operator, defined as

$$\langle f\rangle_{\square} = \frac{1}{\left|\Omega^{\mathrm{F}}_{\square}\right|}\int_{\Omega^{\mathrm{F}}_{\square}} f\,\mathrm{d}V \tag{26}$$

4. SOLUTION-BASED SHAPE FUNCTIONS

4.1. Computing discrete shape functions

For the analysis of upper and lower bounds for strong periodicity according to Section 3, we require the velocity or pressure function spaces to contain only strongly periodic functions. In the case of a 2D flow, this can be achieved using global quadratic shape functions along the fluid part of the boundary (cf. [12]). However, in 3D, there is no apparent way of producing global shape functions for that purpose, as the arbitrary geometry is in 2D. To that end, we introduce the concept of solution-based shape functions being global base functions that are produced by manipulating a possibly non-periodic solution of a Stokes flow. If these base functions are strongly periodic, we have ensured that the resulting flow is indeed also strongly periodic.

As the discussed method is used to create solution spaces for both velocity and pressures and because the procedure is the same for both, we introduce the loosely defined function spaces $\mathcal{Q}_{\square}$ and $\mathcal{Q}'_{\square}$, which we can switch for its velocity or pressure counterparts later.

$$\mathcal{Q}_{\square} = \left\{q : q \text{ is sufficiently regular and satisfies Dirichlet conditions on } \Omega^{\mathrm{F}}_{\square}\right\} \tag{27a}$$

$$\mathcal{Q}'_{\square} = \left\{q : q\in\mathcal{Q}_{\square}, [\![q]\!] = 0 \text{ on } \Gamma^{\mathrm{F}+}_{\square}\right\} \subset \mathcal{Q}_{\square}. \tag{27b}$$

DOI: 10.1002/nme

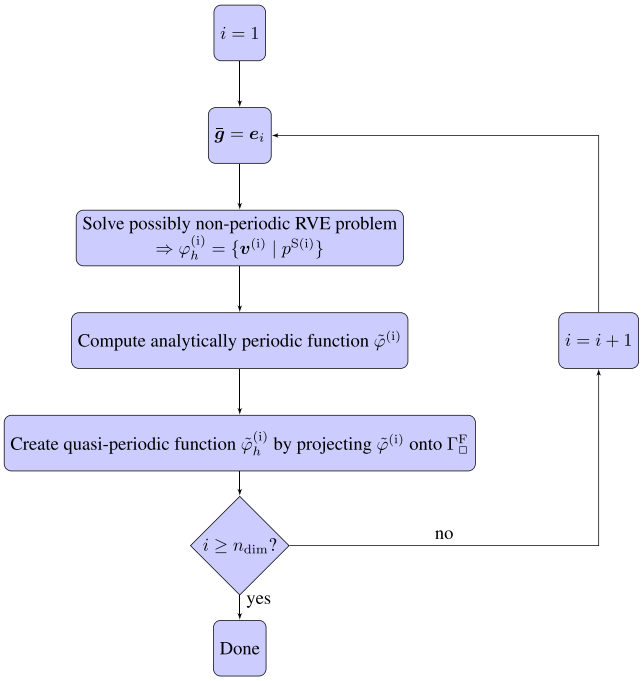

Figure 2. Flowchart for producing solution-based shape function $\tilde{\varphi}_h$.

We also introduce the function $\varphi_h \in \mathcal{Q}_\square$ being either the discrete pressure or velocity field. Here, we restrict ourselves to use the same number of solution-based shape functions as the number of spatial dimensions of the problem, n_{dim}.

For clarity, the following procedure is shown in the flowchart in Figure 2. As a starting point, we solve a Stokes flow on $\Omega_\square^{\mathrm{F}}$ where a unit pressure gradient $\bar{\boldsymbol{g}} = \boldsymbol{e}_i$ is applied. The index $i = 1, \ldots, n_{\mathrm{dim}}$ indicates the spatial direction of the pressure gradient. The discrete solution to this problem is denoted $\varphi_h^{(\mathrm{i})}$, being either the velocity solution $\boldsymbol{v}^{(i)}$ or the pressure solution $p^{\mathrm{S}(\mathrm{i})}$. Naturally, $\varphi_h^{(\mathrm{i})}$ must satisfy all Dirichlet conditions in order to qualify as a proper global base function.

From here, we use the discrete $\varphi_h^{(\mathrm{i})}$ (cf. Figure 3(a)) to produce an analytically periodic function $\tilde{\varphi}^{(\mathrm{i})} \in \mathcal{Q}'_\square$ (cf. Figure 3(b)) by computing the average of $\varphi_h^{(\mathrm{i})}$ as

$$\tilde{\varphi}^{(\mathrm{i})}(\boldsymbol{x}) = \frac{\sum_{j=1}^{n} \varphi_h^{(\mathrm{i})}\left(\boldsymbol{x}_j^{\mathrm{m}}(\boldsymbol{x})\right)}{n} \tag{28}$$

where n is the number of mirror points for a point on $\Gamma_\square^{\mathrm{F}}$ and $\boldsymbol{x}_j^{\mathrm{m}}$ is an operator such that $\boldsymbol{x}_j^{\mathrm{m}}(\boldsymbol{x})$ is the jth mirror point of $\boldsymbol{x}$. We note that the number of mirror points varies over the cubic domain. For instance, on a surface, there are two mirror points, one on $\Gamma_\square^{\mathrm{F}+}$ and one on the opposite side $\Gamma_\square^{\mathrm{F}-}$. On an edge of a 3D cube, there are four mirror points, and on a corner, there are eight mirror points, as shown in Figure 4.

By projecting the analytically periodic function $\tilde{\varphi}^{(\mathrm{i})}$ onto the discretized boundary $\Gamma_\square^{\mathrm{F}}$, we create a quasi-periodic function $\tilde{\varphi}_h^{(\mathrm{i})}$ with an error in periodicity up to that introduced by the discretization of the boundary. More specifically, the value of $\tilde{\varphi}_h^{(\mathrm{i})}$ in coordinates of nodes is exactly $\tilde{\varphi}^{(\mathrm{i})}$ and is otherwise interpolated using the base functions pertinent to the discretization for that particular function. That is, in the case of Taylor–Hood elements, if $\tilde{\varphi}^{(\mathrm{i})}$ represents the velocity, it is interpolated using quadratic base functions, and if $\tilde{\varphi}^{(\mathrm{i})}$ represents the pressure, it is interpolated using linear base functions.

DOI: 10.1002/nme

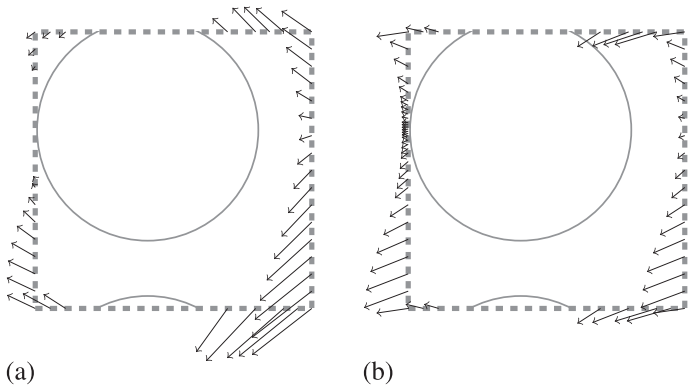

Figure 3. (a) Non-periodic flow $\varphi_h^{(\mathrm{i})}$ along the boundary of an RVE; (b) projection of the analytically periodic function $\tilde{\varphi}^{(\mathrm{i})}$ onto the boundary mesh.

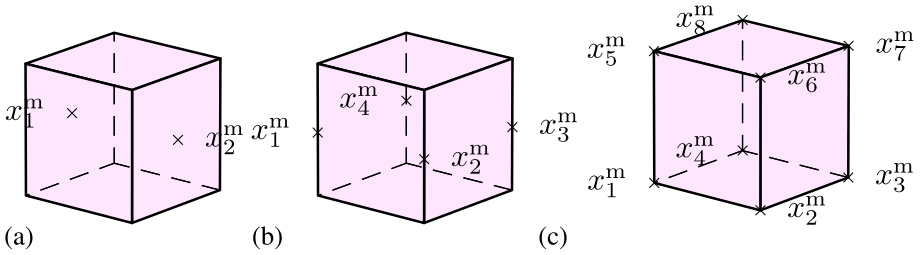

Figure 4. The number of mirror points varies over the domain.

By producing the solution-based shape functions $\tilde{\boldsymbol{v}}_{h,i}$ and $\tilde{p}_{h,i}$, we can now give the velocity and the pressure as

$$\tilde{\boldsymbol{v}}_h = \sum_{i=1}^{n_{\mathrm{dim}}} a_i \tilde{\boldsymbol{v}}_{h,i} \tag{29}$$

and

$$\tilde{p}_h = \sum_{i=1}^{n_{\mathrm{dim}}} b_i \tilde{p}_{h,i} \tag{30}$$

where $a_i \in \mathbb{R}$ and $b_i \in \mathbb{R}$ are arbitrary weights. Furthermore, we note that because both $\tilde{\boldsymbol{v}}_{h,i}$ and $\tilde{p}_{h,i}$ tend to strong periodicity as the fineness of the mesh increases, so does both $\tilde{\boldsymbol{v}}_h$ and $\tilde{p}_h$.

As a concluding remark, we note that as $\boldsymbol{v}$ in Equation (21) and p^{S} in Equation (22) tend to strong periodicity, the respective bounds approach the strongly periodic energy content. Thus, we can use weak periodic boundary conditions on the RVE problem pertinent to the production of $\varphi_h^{(\mathrm{i})}$ in order to enhance the bound.

4.2. Special case of incompressibility

In the case where we choose to use solution-based shape functions on the velocity field, projecting the analytically periodic function $\tilde{\boldsymbol{v}}$ onto $\Gamma_{\square}^{\mathrm{F}}$ may introduce compressibility into the model because of non-periodicity of the mesh. This implies a violation of the incompressibility condition. In order to compensate for such an error, we compute correction factors that are used to scale the prescribed velocity on $\Gamma_{\square}^{\mathrm{F}+}$ and $\Gamma_{\square}^{\mathrm{F}-}$. As a first step, we split the solution-based shape function $\tilde{\boldsymbol{v}}_h$ into three parts as

$$\tilde{\boldsymbol{v}}_h = \tilde{\boldsymbol{v}}_h^0 + \tilde{\boldsymbol{v}}_h^+ + \tilde{\boldsymbol{v}}_h^- \tag{31}$$

DOI: 10.1002/nme

where $\tilde{\boldsymbol{v}}_h^+$ and $\tilde{\boldsymbol{v}}_h^-$ are the parts of $\tilde{\boldsymbol{v}}_h$ on $\Gamma_\square^{\mathrm{F}+}$ and $\Gamma_\square^{\mathrm{F}-}$, respectively, while $\tilde{\boldsymbol{v}}_h^0$ is the part on $\Gamma_\square^{\mathrm{F}0}$. We can now introduce variables a^+ and a^- such that we weight the terms in Equation (31) as

$$\bar{\tilde{\boldsymbol{v}}}_h = \tilde{\boldsymbol{v}}_h^0 + a^+\tilde{\boldsymbol{v}}_h^+ + a^-\tilde{\boldsymbol{v}}_h^- \tag{32}$$

We want to find a^+ and a^- such that $\bar{\tilde{\boldsymbol{v}}}_h$ is as close to $\tilde{\boldsymbol{v}}$ as possible while maintaining global incompressibility on $\Omega_\square^{\mathrm{F}}$, that is, the same amount of fluid enters and exits the domain. Thus, we state the optimization problem as

$$\min_{\bar{\tilde{\boldsymbol{v}}}_h} \frac{1}{2}\int_{\Gamma_\square^{\mathrm{F}}} \left(\bar{\tilde{\boldsymbol{v}}}_h - \tilde{\boldsymbol{v}}\right)^2 \mathrm{d}S \tag{33a}$$

$$\text{subject to: } \int_{\Gamma_\square^{\mathrm{F}}} \bar{\tilde{\boldsymbol{v}}}_h \cdot \boldsymbol{n}\mathrm{d}S = 0 \tag{33b}$$

In weak form, we state the problem as follows: Find $\left(\bar{\tilde{\boldsymbol{v}}}_h, \lambda\right) \in \mathcal{V}_\square \times \mathbb{Q}_\square$ such that

$$\int_{\Gamma_\square^{\mathrm{F}}} \left(\bar{\tilde{\boldsymbol{v}}}_h - \tilde{\boldsymbol{v}}\right) \delta\bar{\tilde{\boldsymbol{v}}}_h \mathrm{d}S - \lambda \int_{\Gamma_\square^{\mathrm{F}}} \delta\bar{\tilde{\boldsymbol{v}}}_h \cdot \boldsymbol{n}\mathrm{d}S = 0 \qquad \forall \delta\bar{\tilde{\boldsymbol{v}}}_h \tag{34a}$$

$$-\delta\lambda \int_{\Gamma_\square^{\mathrm{F}}} \bar{\tilde{\boldsymbol{v}}}_h \cdot \boldsymbol{n}\mathrm{d}S = 0 \qquad \forall \delta\lambda \tag{34b}$$

By choosing $\delta\bar{\tilde{\boldsymbol{v}}}_h = \left\{\tilde{\boldsymbol{v}}_h^+, \tilde{\boldsymbol{v}}_h^-\right\}$ and $\delta\lambda = 1$, we can solve a^+, a^-, and λ from the following system of equations:

$$\begin{bmatrix} A^+ & 0 & -c^+ \\ 0 & A^- & -c^- \\ -c^+ & -c^- & 0 \end{bmatrix} \begin{bmatrix} a^+ \\ a^- \\ \lambda \end{bmatrix} = \begin{bmatrix} B^+ \\ B^- \\ c^0 \end{bmatrix} \tag{35a}$$

where

$$A^+ = \int_{\Gamma_\square^{\mathrm{F}}} \tilde{\boldsymbol{v}}_h^+ \cdot \tilde{\boldsymbol{v}}_h^+ \mathrm{d}S \qquad A^- = \int_{\Gamma_\square^{\mathrm{F}}} \tilde{\boldsymbol{v}}_h^- \cdot \tilde{\boldsymbol{v}}_h^- \mathrm{d}S \qquad B^+ = \int_{\Gamma_\square^{\mathrm{F}}} \left(\tilde{\boldsymbol{v}} - \tilde{\boldsymbol{v}}_h^0\right) \cdot \tilde{\boldsymbol{v}}_h^+ \mathrm{d}S \tag{36a}$$

$$B^- = \int_{\Gamma_\square^{\mathrm{F}}} \left(\tilde{\boldsymbol{v}} - \tilde{\boldsymbol{v}}_h^0\right) \cdot \tilde{\boldsymbol{v}}_h^- \mathrm{d}S \qquad c^0 = \int_{\Gamma_\square^{\mathrm{F}}} \tilde{\boldsymbol{v}}_h^0 \cdot \boldsymbol{n}\mathrm{d}S \qquad c^+ = \int_{\Gamma_\square^{\mathrm{F}}} \tilde{\boldsymbol{v}}_h^+ \cdot \boldsymbol{n}\mathrm{d}S \tag{36b}$$

$$c^- = \int_{\Gamma_\square^{\mathrm{F}}} \tilde{\boldsymbol{v}}_h^- \cdot \boldsymbol{n}\mathrm{d}S \tag{36c}$$

For completeness, we give the explicit expressions for the unknowns in (35a)

$$a^+ = \frac{B^+c^{-2} - B^-c^-c^+ - A^-c^0c^+}{A^+c^{-2} + A^-c^{+2}} \tag{37a}$$

$$a^- = \frac{B^-c^{+2} - B^+c^-c^+ - A^+c^0c^-}{A^+c^{-2} + A^-c^{+2}} \tag{37b}$$

4.3. Solution-based shape functions on the velocity

For the computation of the upper energy bound discussed in Section 3, we introduce the function space

$$\mathcal{V}_\square' = \left\{ \boldsymbol{v} \in \mathcal{V}_\square : \boldsymbol{v} = \sum_{i=1}^{n_{\mathrm{dim}}} b_i \bar{\tilde{\boldsymbol{v}}}_{h,i} \text{ on } \Gamma_\square^{\mathrm{F}}, b_i \in \mathbb{R} \right\} \subset \mathcal{V}_\square \tag{38}$$

where b_i is an unknown coefficient and $\bar{\tilde{\boldsymbol{v}}}_{h,i}$ is the solution-based shape function arising from a pressure gradient in the direction $\boldsymbol{e}_i$. In order to avoid numerical difficulties relevant to possible compressibility, we define the velocity $\bar{\tilde{\boldsymbol{v}}}_{h,i}$ on $\partial\Omega_\square^{\mathrm{F}}$ as

DOI: 10.1002/nme

$$\bar{\tilde{\boldsymbol{v}}}_{h,i} = \begin{cases} a^+ \tilde{\boldsymbol{v}}_h^{(\mathrm{i})} & \text{on } \Gamma_\square^{\mathrm{F}+} \\ a^- \tilde{\boldsymbol{v}}_h^{(\mathrm{i})} & \text{on } \Gamma_\square^{\mathrm{F}-} \\ \tilde{\boldsymbol{v}}_h^{(\mathrm{i})} & \text{on } \Gamma_\square^{\mathrm{F}0} \end{cases} \tag{39}$$

where the correction factors a^+ and a^- are defined in Equation (37). We note that, because $\bar{\tilde{\boldsymbol{v}}}_{h,i}$ is strongly periodic, so is $\boldsymbol{v} \in \mathcal{V}'_\square$ and $c_\square(\boldsymbol{v}, \boldsymbol{\beta}) = 0$ for any $\boldsymbol{\beta} \in \mathcal{B}_\square$. The formulation of the problem is now as follows: Find $(\boldsymbol{v}, p^{\mathrm{S}}, \gamma) \in \mathcal{V}'_\square \times \mathcal{P}^{\mathrm{S}}_\square \times \mathcal{G}_\square$ such that

$$a_\square(\boldsymbol{v}; \delta\boldsymbol{v}) - b_\square(\delta\boldsymbol{v}, p^{\mathrm{S}}) = -e_\square(\delta\boldsymbol{v}, \bar{\boldsymbol{g}}) \qquad \forall \delta\boldsymbol{v} \in \mathcal{V}'_\square \tag{40a}$$

$$-b_\square(\boldsymbol{v}, \delta p^{\mathrm{S}}) - d_\square(\delta p^{\mathrm{S}}, \gamma) = 0 \qquad \forall \delta p^{\mathrm{S}} \in \mathcal{P}^{\mathrm{S}}_\square \tag{40b}$$

$$-d_\square(p^{\mathrm{S}}, \delta\gamma) = 0 \qquad \forall \delta\gamma \in \mathcal{G}_\square \tag{40c}$$

In the finite element setting, $\mathcal{V}'_\square$ is simply constructed by defining the global basis functions pertaining to $\bar{\tilde{\boldsymbol{v}}}_{h,i}$ on the nodes residing on $\Gamma^{\mathrm{F}}_\square$.

4.4. Solution-based shape functions for the pressure

For the lower energy bound, we follow the procedure described in Section 4.3 and introduce the function space

$$\mathcal{P}^{\mathrm{S}\,\prime}_\square = \left\{ \tilde{p}_h \in \mathcal{P}^{\mathrm{S}}_\square : \tilde{p}_h = \sum_{i=1}^{n_{\mathrm{dim}}} a_i \tilde{p}_{h,i} \text{ on } \Gamma^{\mathrm{F}}_\square, a_i \in \mathbb{R} \right\} \subset \mathcal{P}^{\mathrm{S}}_\square \tag{41}$$

where a_i is an unknown coefficient and $\tilde{p}_{h,i}$ is the solution-based shape function pertinent to the ith spatial direction.

As the pressure is strongly periodic, we have $d_\square(p^{\mathrm{S}}, \gamma) = 0$ for any $p^{\mathrm{S}} \in \mathcal{P}^{\mathrm{S}\,\prime}_\square$ and $\gamma \in \mathcal{G}_\square$. Thus, we state the problem on weak form, as follows: Find $(\boldsymbol{v}, p^{\mathrm{S}}, \boldsymbol{\beta}) \in \mathcal{V}_\square \times \mathcal{P}^{\mathrm{S}\,\prime}_\square \times \mathcal{B}_\square$ such that

$$a_\square(\boldsymbol{v}; \delta\boldsymbol{v}) - b_\square(\delta\boldsymbol{v}, p^{\mathrm{S}}) - c_\square(\delta\boldsymbol{v}, \boldsymbol{\beta}) = -e_\square(\delta\boldsymbol{v}, \bar{\boldsymbol{g}}) \qquad \forall \delta\boldsymbol{v} \in \mathcal{V}_\square \tag{42a}$$

$$-b_\square(\boldsymbol{v}, \delta p^{\mathrm{S}}) = 0 \qquad \forall \delta p^{\mathrm{S}} \in \mathcal{P}^{\mathrm{S}\,\prime}_\square \tag{42b}$$

$$-c_\square(\boldsymbol{v}, \delta\boldsymbol{\beta}) = 0 \qquad \forall \delta\boldsymbol{\beta} \in \mathcal{B}_\square \tag{42c}$$

Similarly as for the velocities in Section 4.3, we note that the finite element counterpart of $\mathcal{P}^{\mathrm{S}\,\prime}_\square$ can be constructed by constraining the nodal values of the pressure on $\Gamma^{\mathrm{F}}_\square$ pertinent to $\tilde{p}_{h,i}$.

5. NUMERICAL EXAMPLE

5.1. Preliminaries

In the numerical example, we will investigate the permeability and its upper and lower bounds on a geometrically periodic structure. More specifically, we will investigate how the weak periodic boundary conditions, and the proposed bounds, perform compared with strong periodicity. First, we consider the approximations on fixed discretization (Section 5.2) and later also the behavior of the bounds during refinement of the finite element discretization (Section 5.3).

To this end, we will use a 'quasi-periodic' mesh, which simply means that the surface elements on opposite sides are of similar size. The permeability of the RVE with the quasi-periodic mesh and weak periodic boundary conditions will be compared with two alternative discretizations of the same RVE: (i) a mesh where surface elements on opposing sides are of very different sizes and (ii) a strongly periodic mesh where the sizes of surface elements are approximately the same as those of the quasi-periodic mesh.

As to the geometry of the subscale, we choose to use a body centered cubic (BCC) structure of slightly intersecting spheres as a solid, around which a Stokes flow is present. The material model used for the fluid is the standard linear model presented in Equation (7).

DOI: 10.1002/nme

The RVE is chosen as a unit cell as seen in Figure 5(a). The space occupied by the RVE is chosen in such a way that the $(x; y)$ and the $(x; z)$ planes are planes of symmetry and the RVE window is slightly shifted along the x-axis in order to create a non-symmetric geometry. The distance from the center sphere to the boundary of the RVE is 0.5 in the y and z directions and 0.46 in the x direction at its closest point (cf. Figure 5(b)). The distance between the centers of spheres in the same plane is 1 in the $(x; y)$, $(y; z)$, and $(x; z)$ planes, respectively, and the radius of each spheres is 0.45. The solid phase in the RVE is shown in Figure 5(c).

The shape of the elements in all simulations is tetrahedral, and the discretization is P2–P1, that is, a Taylor–Hood element (quadratic velocity and linear pressure).

For the following numerical example, we define the function spaces for the discretization of the Lagrange multipliers as

$$\mathcal{B}_\square(n_p) = \left\{ \boldsymbol{\beta} \in \mathcal{B}_\square : \boldsymbol{\beta} = \sum_{i=0}^{n_p} \sum_{j=0}^{n_p - i} \boldsymbol{b}_{ij} \xi^i \eta^j \right\} \tag{43a}$$

$$\mathcal{G}_\square(n_p) = \left\{ \gamma \in \mathcal{G}_\square : \gamma = \sum_{i=0}^{n_p} \sum_{j=0}^{n_p - i} g_{ij} \xi^i \eta^j \right\} \tag{43b}$$

where n_p is the order of the polynomial, $\boldsymbol{b}_{ij} \in \mathbb{R}^2$ and $g_{ij} \in \mathbb{R}$ are coefficients, and ξ and η are the local coordinates on the surface of the RVE. As the polynomial depends on two coordinates, note that the number of terms in the expression is $((n_p + 1)^2 + n_p + 1)/2$ if we consider all cross-terms. Furthermore, we choose solution spaces for the velocity and pressure fields according to Section 4.

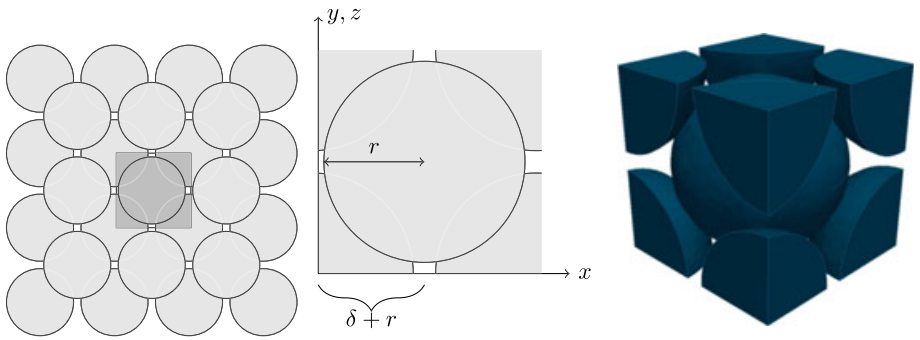

Figure 5. (a) 2D representation of the periodic lattice with the RVE highlighted; (b) position of the RVE window; and (c) 3D representation of the solid phase of the RVE.

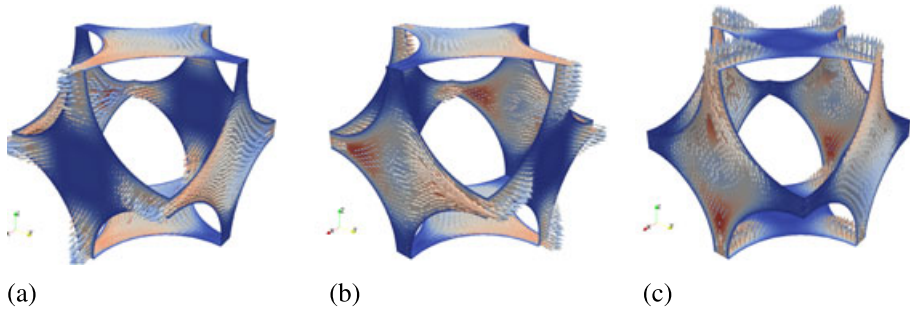

Figure 6. Solution-based shape functions $\bar{\tilde{\boldsymbol{v}}}^{v,4}_{h,1}$, $\bar{\tilde{\boldsymbol{v}}}^{v,4}_{h,2}$, and $\bar{\tilde{\boldsymbol{v}}}^{v,4}_{h,3}$ for the velocity pertinent to macroscopic unit pressure gradients $\bar{\boldsymbol{g}} = \{\boldsymbol{e}_1, \boldsymbol{e}_2, \boldsymbol{e}_3\}$.

DOI: 10.1002/nme

More specifically, we define the following function spaces:

$$\mathcal{P}_{\square}^{\mathrm{S}\,0} = \left\{ p \in H^1\left(\Omega_{\square}^{\mathrm{F}}\right) : p = 0 \text{ on } \Gamma_{\square}^{\mathrm{F}} \right\} \subset \mathcal{P}_{\square}^{\mathrm{S}} \tag{44a}$$

$$\mathcal{P}_{\square}^{\mathrm{S}\,\prime}(n_p) = \left\{ p \in H^1\left(\Omega_{\square}^{\mathrm{F}}\right) : p = \sum_{i=1}^{n_{\mathrm{dim}}} a_i \, \tilde{p}_i^{n_p} \text{ on } \Gamma_{\square}^{\mathrm{F}} \right\} \subset \mathcal{P}_{\square}^{\mathrm{S}} \tag{44b}$$

$$\mathcal{V}_{\square}'(n_p) = \left\{ \boldsymbol{v} \in \left[H^1\left(\Omega_{\square}^{\mathrm{F}}\right)\right]^3 : \boldsymbol{v} = 0 \text{ on } \Gamma_{\square}^{\mathrm{int}}, \boldsymbol{v} = \sum_{i=1}^{n_{\mathrm{dim}}} \boldsymbol{b}_i \, \tilde{\bar{\boldsymbol{v}}}_{h,i}^{v,n_p} \text{ on } \Gamma_{\square}^{\mathrm{F}} \right\} \subset \mathcal{V}_{\square} \tag{44c}$$

where $\tilde{p}_i^{n_p}$ and $\tilde{\bar{\boldsymbol{v}}}_{h,i}^{v,n_p}$ are the solution-based shape functions pertinent to the pressure and velocity fields defined in Sections 4.3 and 4.4. The n_p decoration indicates for the order of the Lagrange multiplier polynomial approximation used when producing the solution-based shape functions. Furthermore, a macroscale unit pressure gradient is imposed on the RVE in each spatial direction, and in the case of velocities, the correction factors presented in Section 4.2 are used. Figure 6 illustrates the solution-based shape functions pertinent to weak periodicity of order 4 in all three spatial directions.

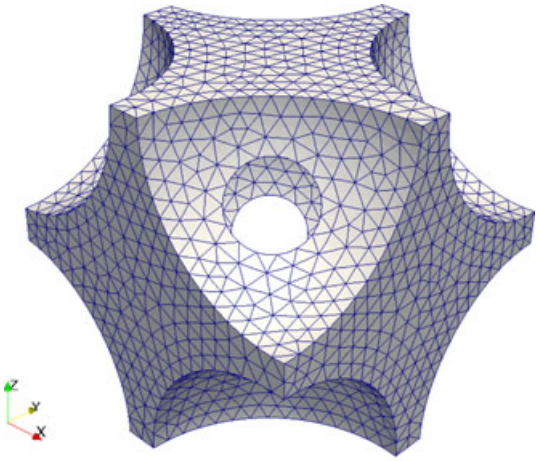

(a)

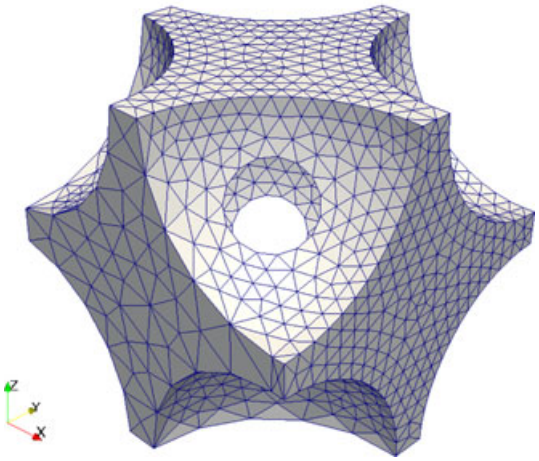

(b)

Figure 7. (a) Quasi-periodic mesh; (b) non-periodic mesh.

DOI: 10.1002/nme

Remark 4

In order to maintain compatibility between the velocity and pressure spaces, we avoid tetrahedral elements located such that all velocity degrees of freedom are either prescribed or hanging on a solution-based shape function. This is solved by flipping the edge between the tetrahedral element and its neighbor such that one node is located inside the volume.

5.2. *Weak approximations and bounds on fixed meshes*

We shall now investigate how the weak periodic boundary conditions and the pertinent bounds converge on fixed finite element discretizations (meshes). The behavior will be studied for fully non-

Table I. Number of volume elements, nodes, and surface elements on respective sides of the representative volume elements.

			Surface elements						
	Volume elements	Nodes	x^+	x^-	y^+	y^-	z^+	z^-	h
Non-periodic	6477	13,002	300	56	294	82	288	56	0.05/0.15
Quasi-periodic	7807	15,744	304	306	296	286	256	290	0.05
Periodic	13,729	24,001	344	344	334	334	342	342	0.05

For the surface elements, the letter and the sign tells which direction the surfaces normally point to. h is the longest allowed edge.

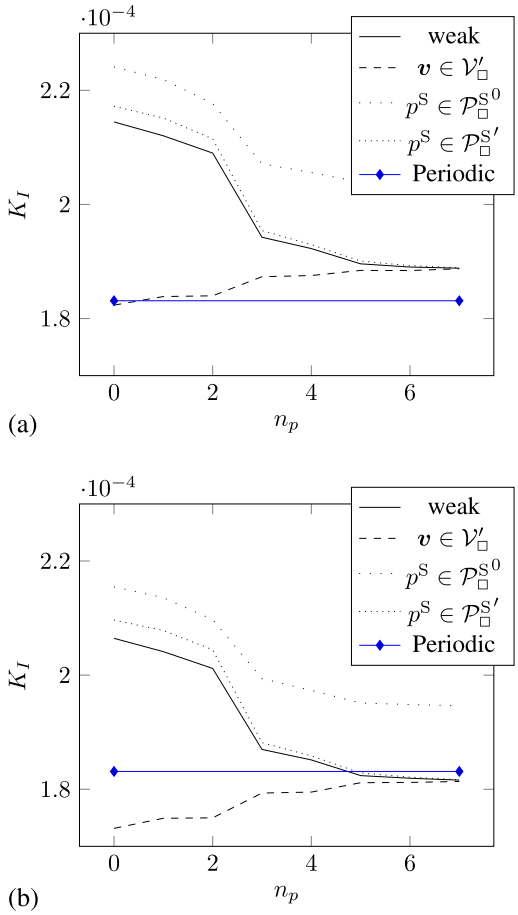

Figure 8. Permeability plots for different choices of solution spaces on (a) non-uniform mesh and (b) quasi-uniform mesh.

DOI: 10.1002/nme

periodic as well as quasi-periodic meshes. Here, quasi-periodic means having elements of similar sizes on opposing sides of the RVE, whereas the fully non-periodic mesh has differently sized elements on opposing sides. For reference, we also consider a strongly periodic mesh with conventional periodic boundary conditions enforced.

As to the discretization of the domain, three meshes are used:

(1) A 'quasi-periodic' mesh with approximately equally sized element on all sides (cf. Figure 7(a)).
(2) A non-periodic mesh with a coarse mesh on the $\Gamma_{\square}^{\mathrm{F}-}$ and a fine mesh on $\Gamma_{\square}^{\mathrm{F}+}$ (cf. Figure 7(b)).
(3) A periodic mesh with the same element sizes as in 1.

Detailed information on the number of nodes and elements for the various meshes is given in Table I.

In order to estimate how the weak periodic boundary conditions converge towards strong periodicity as we increase the order of the polynomial, we evaluate the upper and lower bounds for the permeability. Thus, if the gap between the upper and lower bounds is small, the weak periodicity will perform well. Figure 8 shows how the first eigenvalue K_I of the permeability tensor changes for the quasi-periodic and non-periodic meshes. The same quantity for the strong periodic boundary conditions using the periodic mesh is shown in both plots. Note that the order of all polynomials is the same for each choice of n_p, both when producing the shape functions and for imposing weak periodicity.

We note that the shape of the curves in both plots is similar but the values in Figure 8(a) are higher than that for the strongly periodic solution, while the values in Figure 8(b) are lower. These differences arise from the different approximations induced by the individual meshes (cf. the subsequent convergence study in Section 5.3). We see that K_I for the strongly periodic solution is closer to K_I for the quasi-periodic mesh with high n_p as compared with the non-periodic one. This is expected because the periodic and quasi-periodic meshes are of similar size.

Figure 9 shows the velocity field in a cross-section of the RVEs with weak periodic boundary conditions. The pressure fields for the same solutions are shown in Figure 10. Finally, for the non-

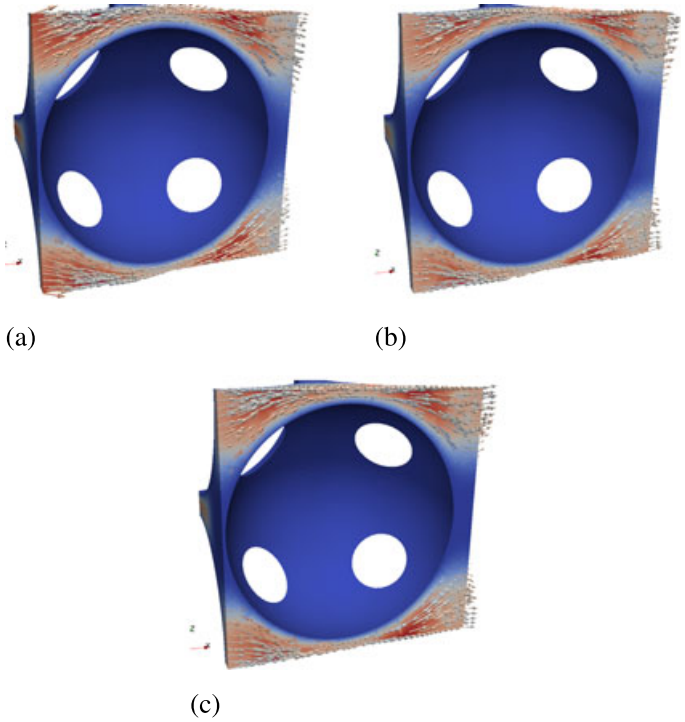

Figure 9. Velocities resulting from (a) zeroth order; (b) third order; and (c) seventh order.

DOI: 10.1002/nme

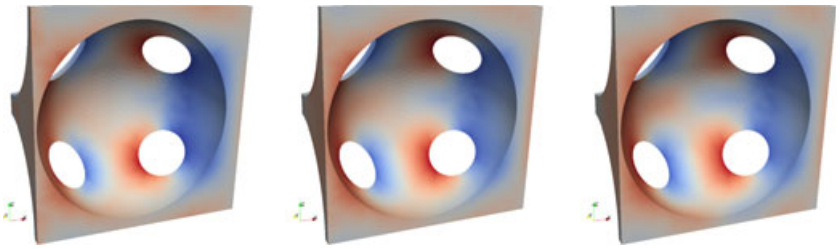

(a) (b) (c)

Figure 10. Pressure resulting from (a) zeroth order; (b) third order; and (c) seventh order.

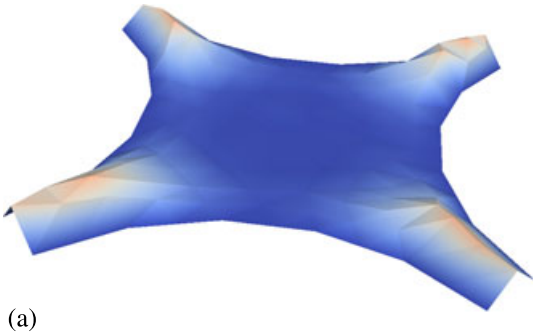

(a)

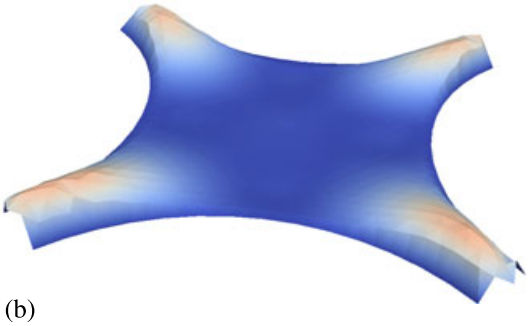

(b)

Figure 11. Velocity on non-uniform mesh (a) $\Gamma_{\square}^{\mathrm{F}-}$ and (b) $\Gamma_{\square}^{\mathrm{F}+}$.

periodic mesh, Figure 11 shows the velocity field on the coarse mesh on $\Gamma_{\square}^{\mathrm{F}-}$ and the fine mesh on $\Gamma_{\square}^{\mathrm{F}+}$. Both the deformation and the color represent the velocity.

In order to investigate the accuracy of lower-order shape functions with higher-order weakly periodic boundary conditions, we introduce the parameter n_p^s as the order of the shape function. We will now hold n_p^s constant and let n_p vary. From here, we can compute an upper bound by choosing the velocity and pressures in the following way:

$$p^{\mathrm{S}} \in \mathcal{P}_{\square}^{\mathrm{S}\,\prime}\left(n_p^s\right), \qquad \boldsymbol{v} \in \mathcal{V}_{\square}, \qquad \boldsymbol{\beta} \in \mathcal{B}(n_p) \tag{45}$$

and for the lower bound

$$p^{\mathrm{S}} \in \mathcal{P}_{\square}^{\mathrm{S}}, \qquad \boldsymbol{v} \in \mathcal{V}_{\square}'\left(n_p^s\right), \qquad \gamma \in \mathcal{G}(n_p) \tag{46}$$

Figure 12 shows the highest eigenvalue of the permeability tensor for different choices of n_p^s. We note that because of the procedure pertinent to the computation of the solution-based shape functions, there is no guarantee that the energy decreases as n_p^s increases. This is shown in Figure 12

DOI: 10.1002/nme

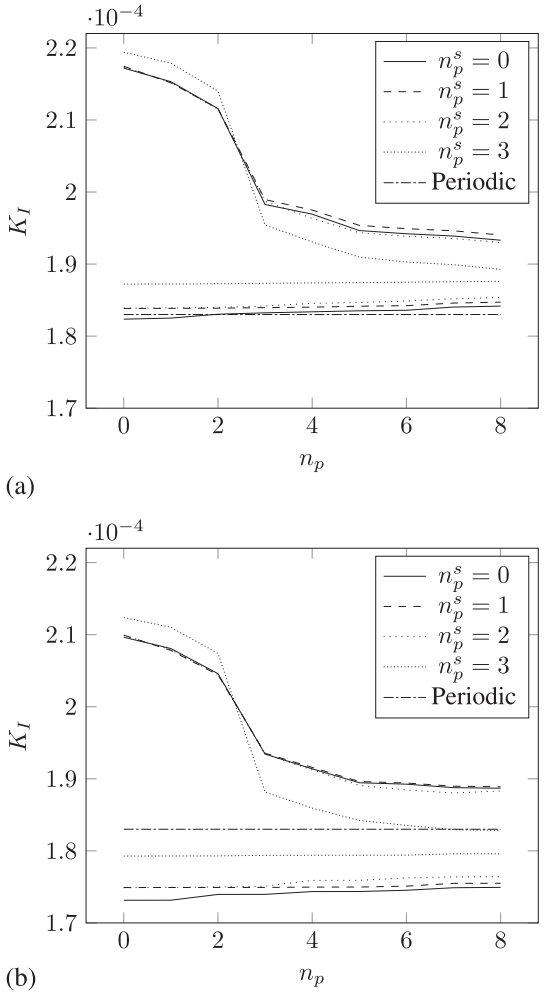

Figure 12. Plots show how the highest eigenvalue of the upper and lower bounds for the permeability for different choices of solution spaces changes on a (a) Non uniform mesh (b) Quasi-uniform mesh.

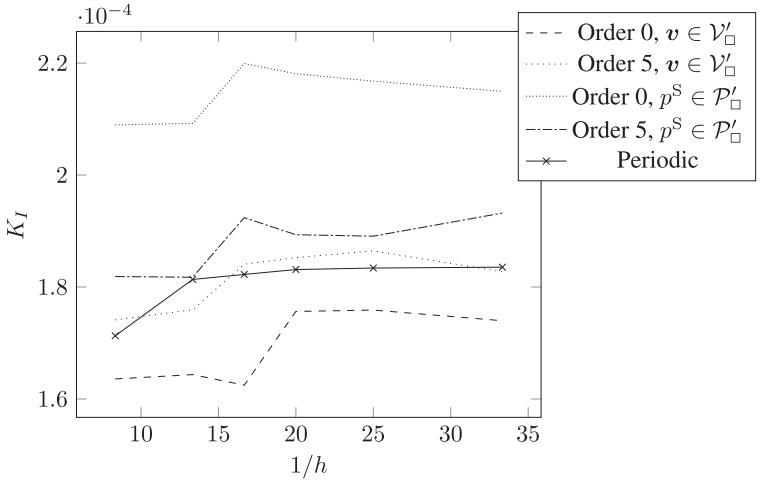

Figure 13. Plot shows how bounds calculated using weak periodicity of order 0 and 5 vary with mesh fineness. Here, h is the maximum allowed length of an element edge.

DOI: 10.1002/nme

where the upper bound does not decrease monotonically. The same quantity for the strongly periodic boundary conditions using the periodic mesh is shown in both plots. Again, we note the fact that the strongly periodic solution is not within all bounds due to different meshes used.

5.3. Convergence of bounds with mesh refinement

Finally, to demonstrate how the bounds behave as the mesh is refined, we compute K_I for meshes with various choices of largest allowed length h of an element edge and varying orders of weak periodicity when computing the solution-based shape functions. We compare the resulting bounds with the strongly periodic solutions of a mesh of similar size. The results are shown in Figure 13. Note that the meshes are of similar size only; hence, there is no guarantee that the strong periodic solution should be contained within the bounds (as indeed is the case for some choices of h). However, as h decreases, the solution tends to a value within the bounds.

6. CONCLUSIONS AND OUTLOOK

In this paper, we have shown a novel approach on how to compute upper and lower energy bounds for flow through porous materials from a saddle point problem. In the case of a linear flow, upper and lower bounds on the permeability are computed, and with the use of these bounds, we have also evaluated the performance on weak periodicity and shown that they perform well, at least for higher-order approximations of the Lagrange multipliers.

The bounds were computed using global base functions for the velocity and pressure using solutions-based shape functions, pertaining from the solution of a Stokes flow that is then processed to produce a strongly periodic base function. Correction factors due to possible compressibility in the otherwise incompressible flow are also discussed.

In the numerical section, we have shown that the use of solution-based shape functions is suitable to use on both quasi-periodic as well as non-periodic meshes and that the bounds converge as the flux and traction required for weak periodicity increase are refined. This implies that we can replace the strongly periodic boundary conditions with weak ones of sufficiently high-order of approximation.

As a suggestion for future work using solutions-based shape functions, an evaluation of the use of this technique for the Dirichlet boundary condition for the Stokes flow in this type of application should be done. This would enable us to compute upper and lower bounds for a non-periodic microstructure.

An important issue in computations involving porous materials is that of the coupling between permeability and deformation; a framework for a variationally consistent model that takes this coupling into consideration is of great interest.

REFERENCES

1. Arbogast T, Lehr H. Homogenization of a Darcy–Stokes system modeling vuggy porous media. *Computational Geosciences* 2006; **10**(3):291–302.
2. Ohman M, Runesson K, Larsson F. Computational mesoscale modeling and homogenization of liquid-phase sintering of particle agglomerates. *Technische Mechanik* 2011; **32**:463–483.
3. Ngo ND, Tamma KK. Microscale permeability predictions of porous fibrous media. *International Journal of Heat and Mass Transfer* 2001; **44**(16):3135–3145.
4. Pillai KM, Advani SG. Numerical and analytical study to estimate the effect of two length scales upon the permeability of a fibrous porous medium. *Transport in Porous Media* 1995; **21**(1):1–17.
5. Nilenius F, Larsson F. Macroscopic diffusivity in concrete determined by computational homogenization. *International Journal for Numerical and Analytical Methods in Geomechanics* 2012; **2012**:1535–1551.
6. Geers MGD, Kouznetsova VG, Brekelmans WAM. Multi-scale computational homogenization: trends and challenges. *Journal of Computational and Applied Mathematics* 2010; **234**(7):2175–2182.
7. Sánchez-Palencia E. *Non-homogeneous Media and Vibration Theory*. Springer: Berlin Heidelberg, 1980. ISBN: 3-540-10000-8.
8. Allaire G. Homogenization of the Stokes flow in a connected porous medium. *Asymptotic Analysis* 1989; **2**:203–222.
9. Hornung U. *Homogenization and Porous Media*. Springer: Berlin Heidelberg, 1997. ISBN: 0-387-94786-8.
10. Rubinstein J, Torquato S. Flow in random porous media: mathematical formulation, variational principles, and rigorous bounds. *Journal of Fluid Mechanics* 1989; **206**:25–46.

DOI: 10.1002/nme

11. Berryman JG. Computing variational bounds for flow through random aggregates of spheres. *Journal of Computational Physics* 1983; **52**(1):142–162.
12. Sandström C, Larsson F, Runesson K. Weakly periodic boundary conditions for the homogenization of flow in porous media. *Advanced Modeling and Simulation in Engineering Sciences* 2014; **1**(1):12.
13. Hughes T. Multiscale phenomena: Green's functions, the Dirichlet-to-Neumann formulation, subgrid scale models, bubbles and the origins of stabilized methods. *Computer Methods in Applied Mechanics and Engineering* 1995; **127**(1-4):387–401.
14. Hughes TJR, Feijóo GR, Mazzei L, Quincy JB. The variational multiscale method – a paradigm for computational mechanics. *Computer Methods in Applied Mechanics and Engineering* 1998; **166**:3–24.
15. Liu X, Li S. A variational multiscale stabilized finite element method for the Stokes flow problem. *Finite Elements in Analysis and Design* 2006; **42**(7):580–591.
16. Larsson F, Runesson K, Su F. Variationally consistent computational homogenization of transient heat flow. *International Journal for Numerical Methods in Engineering* 2009; **81**(13):1659–1686.
17. Sandström C, Larsson F. Variationally consistent homogenization of Stokes flow in porous media. *International Journal for Multiscale Computational Engineering* 2013; **11**(2):117–138.
18. Nguyen VD, Béchet E, Geuzaine C, Noels L. Imposing periodic boundary condition on arbitrary meshes by polynomial interpolation. *Electrical Engineering* 2011; **55**(November):390–406.

DOI: 10.1002/nme